


## Gamma instability in an inhomogeneous environment and salt-fingering staircase trapping: Determining the step size

Yuchen Ma<sup>1</sup> and W. R. Peltier<sup>1</sup>*University of Toronto, 60 St. George Street, Toronto, Canada* (Received 14 November 2020; accepted 17 February 2021; published 17 March 2021)

Gamma ( $\gamma$ ) instability theory, originally proposed in 2003, continues to provide the most promising explanation of salt-fingering engendered thermohaline staircases that are ubiquitously present in both the global ocean and lakes. Our purpose herein is to extend  $\gamma$  instability theory to salt-fingering systems in which the vertical gradients of temperature and salinity are not constant. Our goal is to explain why the characteristic “step size” in a salt-fingering staircase is larger in regions characterized by weak gradients. Through application of an appropriately modified linear stability analysis, we first demonstrate that the most quickly growing mode of instability is unaltered by the inhomogeneity of the background stratification in most cases. We then perform numerical simulations based upon the mean field equations to show that staircases tend to form and thereafter merge much more quickly in the low gradient regions than the high gradient regions. After explaining this difference of timescale within the framework of our model, we argue that the differences in background gradients of physical properties may arise naturally in a quasiequilibrium staircase environment. We further invoke observations from the Tyrrhenian Sea to support a quasiequilibrium staircase hypothesis.

DOI: [10.1103/PhysRevFluids.6.033903](https://doi.org/10.1103/PhysRevFluids.6.033903)

### I. INTRODUCTION

Thermohaline staircases are some of the most mysterious regular structures observed in all of physical oceanography, structures that exist in vast areas of the oceans including both tropical and polar regions. These structures consist of a series of vertically well-mixed layers separated by sharp density interfaces. There are generally two types of staircases, depending on the sense of the vertical gradients of temperature and salinity of the background in which they occur. The first type of staircase forms primarily in the main thermocline in the low-latitude or mid-latitude ocean where warm salty water lies above relatively colder and fresher water, as has been observed in the Mediterranean Sea [1], Tyrrhenian Sea [2], and the western tropical Atlantic [3,4]. The second type of staircase forms in the opposite environment, where cold and fresh water lies above relatively warmer and saltier water. Observational examples of such staircases can be found in the Arctic Ocean, e.g., Ref. [5], the Weddell Sea, e.g., Ref. [6], offshore Antarctica, e.g., Refs. [7,8], and a variety of lakes in very different environments, e.g., Refs. [9,10].

Although it has been clear for some time that the formation of these two types of staircases are closely related to the two types of double-diffusive instability corresponding to salt fingering and diffusive convection respectively, the detailed mechanism through which layer formation occurs remains a subject of active debate. In fact, the existing literature of attempts to develop a complete theory may be divided into as many as six different lines of argument, which have been summarized in Chapter 8 of Ref. [11]. Among these different explanations, the  $\gamma$  instability theory proposed in

---

\*Corresponding author: [yc.ma@mail.utoronto.ca](mailto:yc.ma@mail.utoronto.ca)

Ref. [12] appears to provide at least the central ingredient of what could become a complete theory to fully explain the formation of salt-fingering staircases (much more significant issues remain concerning the mechanism underlying the formation of the diffusive convection staircases [11]). The  $\gamma$  instability theory of Ref. [12] suggests that uniform salt-fingering fields will be unstable to staircase formation as long as the flux ratio  $\gamma$  ( $\gamma = \overline{w'\Theta'}/\overline{w'S'}$ ) is a decreasing function of density ratio  $R_\rho$  ( $R_\rho = \Theta_z/S_z$ ), which is the dominant nondimensional parameter governing the behavior of the salt-fingering system. Studies using direct numerical simulation (DNS) [13,14], mean field model-based simulations [12,15], and basin-scale general circulation model-based analyses [16] have all demonstrated that the staircase structure will emerge spontaneously if and only if the decreasing  $\gamma(R_\rho)$  criterion is satisfied.

In Ref. [15], it was further suggested that these initially formed staircases are susceptible to an additional (tertiary) instability that drives adjacent layers to merge so as to produce larger scale steps. This mechanism has come to be referred to as involving a “B merger” mechanism, a phenomenon that occurs in a range of nonlinear systems well beyond those involving double diffusion [17]. This mechanism has been analyzed using both numerical simulations [13–15] and observational evidence obtained from ice-tethered profilers (ITPs) in the Arctic Ocean [5,18]. While  $\gamma$  instability theory and the theory of layer merger together form a complete theoretical framework explaining simulations and observations of salt-fingering staircases, the theory suffers from a flaw: the existence of an ultraviolet catastrophe in that the growth rate predicted by the  $\gamma$  instability diverges to infinity as the vertical wave number increases (we will discuss this issue in detail in what follows).

Despite the significant success of  $\gamma$  instability theory, it has been formulated only to describe a system with constant vertical gradients of temperature and salinity. In the work described herein, we will extend the scope of current theory so that it may be applied to a more general system that includes inhomogeneity of vertical gradients. As we will show, this inhomogeneity may be the dominant factor in determining the depth of individual steps in the staircase: The staircase step sizes are always observed to be smaller at vertical positions of relatively higher gradients than at vertical positions characterized by relatively lower gradients. This trend is quite clear in the observational data of both salt-fingering staircases and diffusive convection staircases (see Fig. 2 of Ref. [3], Fig. 1 of Ref. [4], Fig. 11 of Ref. [2], Fig. 8 of Ref. [5], and Fig. 3 of Ref. [6] for examples), but there has not been any entirely satisfactory explanation of this. The only related discussion in the literature appears to consist of the description of staircases in the northwestern Weddell Sea of Antarctica [6], in which the authors of Ref. [19] refer to the small steps in the higher gradient regions as type A steps and the large steps in the lower gradient regions as type B steps [19]. The ensuing work of Ref. [20] attributed the differences in the step sizes in these two different types of staircases to the differences in the environment: Type B cases were found to be located in a more pristine environment and were imagined to be closer to equilibrium and therefore to be characterized by larger steps. For staircases that are observed to form in other regions (see the western tropical Atlantic [3,4] and the Tyrrhenian Sea [2] for examples), however, there are no clearly different environmental conditions on the basis of which one might separate different staircase types as exist in the northwestern Weddell Sea. Yet, there are clearly different step sizes in regions characterized by different background gradients of temperature and salinity. What is therefore required, in our opinion, is a more general theory able to explain staircases other than those in the northwestern Weddell Sea. It is clear to us that the theory to be discussed herein will have to be an extension of the  $\gamma$  instability theory, which already well describes the basic mechanism of staircase formation in constant background gradient circumstances that favor salt-fingering instability.

The outline of the analyses to be described in the remainder of this paper will begin in Sec. II with a brief discussion of the flux laws for salt-fingering turbulence deduced from a series of analyses based upon high-resolution DNS in which both the constant and inhomogeneous background gradient models are employed. These analyses will provide results for  $\gamma$  as a function of  $R_\rho$  that will serve as basis for all of the subsequent analyses. In Sec. III, we will first provide a brief review of the original framework of  $\gamma$  instability theory proposed in Ref. [12], which will be followed by a linear stability analysis based upon the required formulation of this theory which incorporates

the inhomogeneity of the vertical environment. In the subsequent section, Sec. IV, we develop a mean-field-based parametrized model that will be employed to simulate the dynamics of the system after the perturbations develop beyond the linear regime. The discussion of the results obtained on the basis of these analyses focuses upon the key mechanism that controls the evolution of the system. The final step in our discussion of the results of our mean field simulations is to connect them to the ocean observations. A summary of the results obtained in this work and conclusion are offered in Sec. V.

## II. FLUX LAWS FOR THREE-DIMENSIONAL SALT-FINGERING TURBULENCE BASED UPON HIGH-RESOLUTION DIRECT NUMERICAL SIMULATION

The  $\gamma$  instability theory described in Ref. [12] was developed on the basis of the stability characteristics of a set of mean-field equations for temperature and salinity. These mean-field equations were based on the characteristics of the fluxes of heat and salt that were obtained on the basis of high-resolution DNS of doubly diffusive salt-fingering turbulence. Specifically, the flux law employed in Ref. [12] was based on a set of two-dimensional (2D) DNS of relatively low-resolution salt-fingering turbulence simulations [21]. Two decades later, the computational power on the basis of which such simulations may be performed has significantly increased. This has made it possible to perform the needed simulations on the basis of which the flux laws are determined in three spatial dimensions and at much higher resolution; for examples of such work, see Refs. [22–24]. In this section, we will provide a brief summary of the most recent such DNS simulations of Ref. [24] as well as flux laws obtained from them, which will be employed for the purpose of our mean field analyses to follow in the remainder of the paper.

In Ref. [24], 10 three-dimensional DNS simulations were performed in the system characterized by uniform background temperature and salinity gradients with  $R_\rho$  almost evenly distributed in the range of 1.1–10. A visualization of the results obtained in these simulations is provided in the snapshots of the temperature and salinity fields at different stages in the evolution of the turbulent flow in Fig. 1. The results reported in Ref. [24] were the first to describe a methodology that could be employed to distinguish between irreversible and reversible mixing in a doubly diffusive system, this being a critical distinction when turbulent mixing is to be represented in terms of an effective turbulent diffusivity as it is only the irreversible component of mixing that may contribute to this diffusivity. The results of these analyses for the equilibrium irreversible diapycnal diffusivities for heat  $K_\Theta^{irr}$  and for salt  $K_S^{irr}$  [which do not differ significantly from the traditionally diffusivities defined for heat flux  $\overline{w'\Theta'}$  and salt flux  $\overline{w'S'}$  in the equilibrium stage of salt-fingering turbulence (see Ref. [24])] as well as for the irreversible flux ratio  $\gamma^{irr}$  were averaged across the domain and the results obtained from the totality of these simulations are plotted as a function of  $R_\rho$  in Fig. 2. The functional relationship for  $K_\Theta^{irr}(R_\rho)$  and  $\gamma^{irr}(R_\rho)$  were then fit to obtain the following functional forms:

$$\begin{aligned} K_\Theta^{irr} &= \frac{a}{(R_\rho - 1)^b R_\rho^c} \kappa_\theta, \quad (a = 78.09, b = 0.52, c = 0.87), \\ \gamma^{irr} &= aR_\rho^3 + bR_\rho^2 + cR_\rho + d, \quad (a = -0.00068, b = 0.0163, c = -0.125, d = 0.77), \\ K_S^{irr} &= K_\Theta^{irr} R_\rho / \gamma^{irr} \end{aligned} \quad (1)$$

in which  $\kappa_\theta$  is the molecular diffusivity for heat. These empirical parametrizations of the salt-fingering fluxes were tested in Ref. [24] in a further set of DNS simulations using the interface model. Specifically, in DNS simulations that are initialized with hyperbolic-tangent shape profiles for temperature and salinity, it was shown to deliver a correct depth dependence of turbulence intensity in the quasiequilibrium state. The fluxes for heat and salt were shown to adhere locally to expectations based upon the empirical representation of the fluxes from the constant gradient simulations as described by (1), when the depth dependence of  $R_\rho$  at equilibrium in the interface model was taken into account. This fact confirms the validity of the mean-field equation that we will

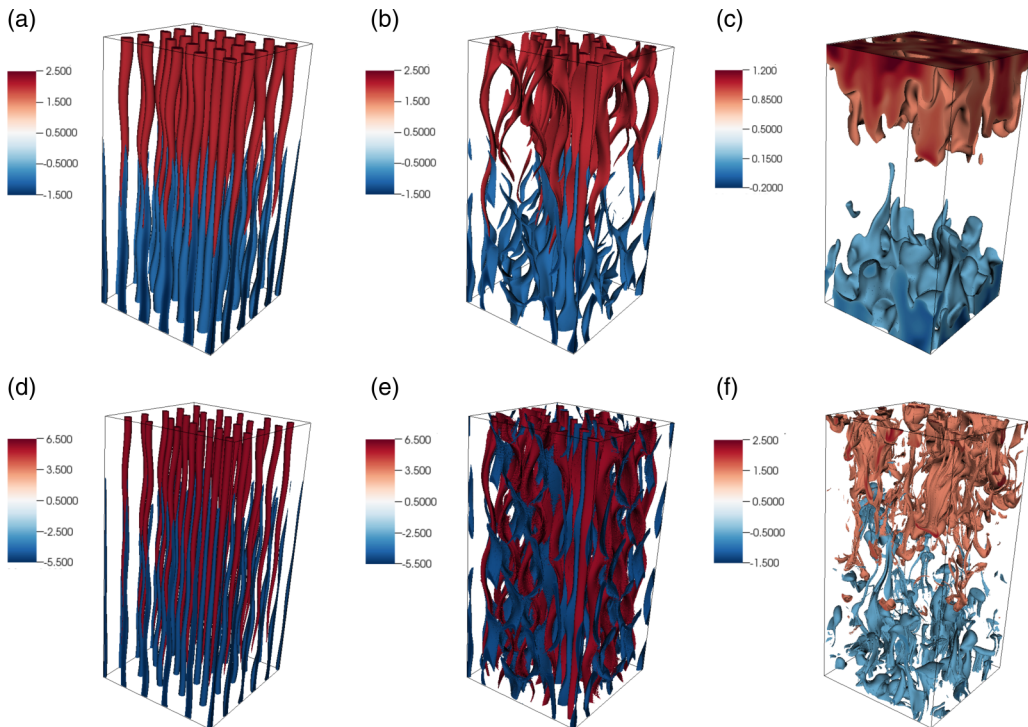


FIG. 1. Volume rendered temperature fields (a)–(c) and salinity fields (d)–(f) at nondimensional times 0.00507, 0.00512, and 0.00766 in the DNS simulation at  $R_\rho = 2$  using the unbounded gradient model in Ref. [24]. A comparison of temperature and salinity fields at these different time slices clearly display the process that causes the salt fingers to break under the action of the secondary zigzag instability [25] and to eventually evolve into a fully turbulent state.

use throughout this paper, especially in the case of an inhomogeneous system that is the primary focus of discussion in what is to follow.

### III. GAMMA-INSTABILITY ANALYSIS IN A VERTICALLY INHOMOGENEOUS ENVIRONMENT

In this section, we will begin by developing a theoretical framework for  $\gamma$  instability theory in a vertically inhomogeneous environment using the mean field equation which is based on the flux laws (1). For the sake of completeness, we will first provide a brief review of the  $\gamma$  instability theory originally formulated in Ref. [12]. We then discuss how the theory must be modified to account for the depth variation of background vertical gradients for temperature and salinity.

#### A. Classical gamma instability theory in the unbounded gradient model

The classical  $\gamma$  instability has been described expeditiously in Ref. [12]. Consider the governing equations for the mean field temperature  $\Theta(z, t)$  and salinity  $S(z, t)$  that are averaged over space and timescales that greatly exceed those characteristic of the salt-fingering instability to obtain

$$\begin{aligned} \frac{\partial \Theta}{\partial t} &= -\frac{\partial}{\partial z} F_\Theta, \\ \frac{\partial S}{\partial t} &= -\frac{\partial}{\partial z} F_S, \end{aligned} \quad (2)$$

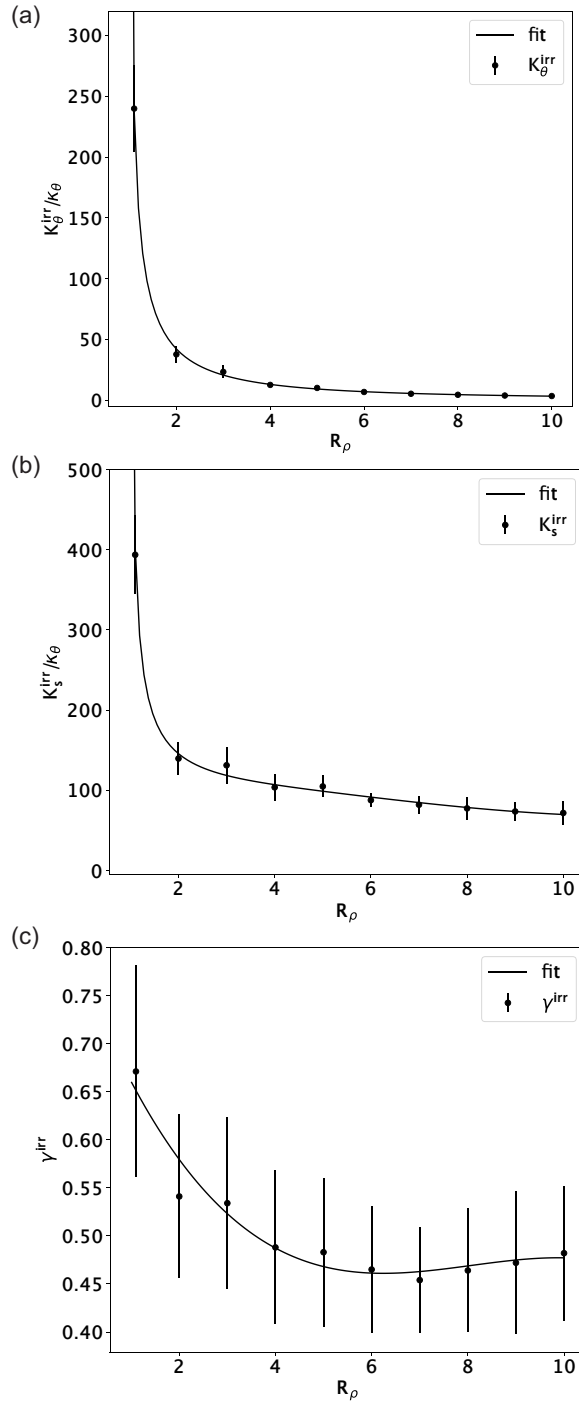


FIG. 2. The averaged irreversible turbulent diapycnal diffusivities for heat (a), for salt (b) as well as irreversible flux ratio (c) as a function of  $R_\rho$  in 10 simulations in the unbounded gradient model [24]. Numerical fitting of (1) is shown in each figure to be compared with the data.

in which the vertical heat and salt fluxes  $F_\Theta$  and  $F_S$  are determined by the relations

$$\begin{aligned} F_\Theta &= -Nu(R_\rho) \frac{\partial \Theta}{\partial z}, \\ F_S &= \frac{F_\Theta}{\gamma(R_\rho)}. \end{aligned} \quad (3)$$

The above equations have been nondimensionalized based on the typical salt-fingering length scale  $d = (\frac{\rho_0 \nu \kappa_\theta}{g \bar{\Theta}_z})^{\frac{1}{4}}$  (see Ref. [11], for example, where  $\nu$  is the molecular viscosity) and the timescale is  $d^2/\kappa_\theta$ . Both the temperature field  $\Theta(z, t)$  and the salinity field  $S(z, t)$  are defined in density units so that a linear equation of state can be expressed as  $\rho = \rho_0 + S - \Theta$ . The thermal Nusselt number  $Nu$  and the total flux ratio  $\gamma$  are defined to include the contributions due to molecular diffusion and can be explicitly determined on the basis of the parametrization scheme (1) as

$$\begin{aligned} Nu(R_\rho) &= K_\Theta^{irr}(R_\rho)/\kappa_\theta + 1, \\ \gamma(R_\rho) &= \frac{K_\Theta^{irr}(R_\rho)/\kappa_\theta + 1}{K_S^{irr}(R_\rho)/\kappa_\theta + \tau} R_\rho, \end{aligned} \quad (4)$$

where  $\tau = \kappa_s/\kappa_\theta = 0.01$  is the molecular diffusivity ratio for salt and heat. However, it should be noticed in what follows that a specific form of parametrization is not necessary in determining the basic requirement for  $\gamma$  instability.

Once  $\Theta(z, t)$  and  $S(z, t)$  are perturbed from their background values  $\bar{\Theta}(z) = \Theta_{0z}z$  and  $\bar{S}(z) = S_{0z}z$  by  $\Theta'$  and  $S'$ ,  $R_\rho$  will also deviate from the background value  $R_{\rho 0} = \Theta_{0z}/S_{0z}$ , namely as

$$\begin{aligned} R_\rho &= R_{\rho 0} \frac{1 + \frac{\Theta'_z}{\Theta_{0z}}}{1 + \frac{S'_z}{S_{0z}}} \\ &\approx R_{\rho 0} \left( 1 + \frac{\Theta'_z}{\Theta_{0z}} - R_{\rho 0} \frac{S'_z}{S_{0z}} \right), \end{aligned} \quad (5)$$

where we have made the approximation that only first-order deviations from the mean fields  $\Theta'$  and  $S'$  need be retained. By substituting (3) and (5) into (2) and again retaining only first-order terms, we obtain the following evolution equations for the perturbations to the initial depth-dependent mean fields:

$$\begin{aligned} \frac{\partial \Theta'}{\partial t} &= (A_2 + Nu)\Theta'_{zz} - A_2 R_{\rho 0} S'_{zz}, \\ \frac{\partial S'}{\partial t} &= A_1 Nu \Theta'_{zz} - A_1 Nu R_{\rho 0} S'_{zz} + \gamma^{-1} \frac{\partial \Theta'}{\partial t}, \end{aligned} \quad (6)$$

where  $A_1 = \frac{\partial \gamma^{-1}}{\partial R_\rho} \Big|_{R_{\rho 0}} R_{\rho 0}$  and  $A_2 = \frac{\partial Nu}{\partial R_\rho} \Big|_{R_{\rho 0}} R_{\rho 0}$ . If we further expand the perturbation fields  $\Theta'$  and  $S'$  into normal modes in (6) as  $(\Theta', S') = (\hat{\Theta}, \hat{S}) \exp(\lambda t + ikz)$ , (6) will be transformed into an eigenvalue problem with the eigenvalue  $\lambda$  determined by the quadratic equation

$$\lambda^2 + \lambda \left[ A_2 + Nu(R_{\rho 0}) - A_1 Nu(R_{\rho 0}) R_{\rho 0} - \frac{R_{\rho 0} A_2}{\gamma(R_{\rho 0})} \right] k^2 - A_1 Nu^2(R_{\rho 0}) R_{\rho 0} k^4 = 0 \quad (7)$$

in which  $A_1 > 0$  is a sufficient condition for the existence of a positive root in (7) and thus suggests that an instability of the basic state would exist in this circumstance. Since the condition  $A_1 > 0$  simply implies that  $\gamma(R_\rho)$  is a decreasing function of  $R_\rho$ , this instability was referred to as the “ $\gamma$  instability” in Ref. [12]. Encouraging matches have been found between this  $\gamma$  instability theory and the staircase structures that form in DNS of salt-fingering turbulence, in both two-dimensional (2D) simulations (for example, Ref. [12]) and three-dimensional (3D) simulations (for example, Ref. [13]).

The theory has been further tested in basin-scale staircase-resolving numerical simulations [16], which demonstrate that the staircase structures only merge if the total flux ratio (that takes the turbulent diapycnal diffusivities into account) satisfies the criterion that  $\gamma$  be a decreasing function of  $R_\rho$ . We will refer this as the “ $\gamma$  criterion” in what follows.

### B. Gamma instability analysis in a vertically inhomogeneous system

In this section, our intention is to investigate how the classical theoretical framework of  $\gamma$  instability will vary if the variations of vertical gradients are considered.

We will still represent the temperature and salinity fields as the sum of a background component and a perturbation as in the last subsection, except that the background fields  $\bar{\Theta}_z(z)$  and  $\bar{S}_z(z)$  are now depth dependent. In this case, Eq. (5) in the last section will become

$$\begin{aligned} R_\rho &= \frac{\Theta_z}{S_z} = \frac{\bar{\Theta}_z}{\bar{S}_z} \frac{1 + \frac{\Theta'_z}{\bar{\Theta}_z}}{1 + \frac{S'_z}{\bar{S}_z}} \\ &\approx \bar{R}_\rho \left( 1 + \frac{\Theta'_z}{\bar{\Theta}_z} - \frac{S'_z}{\bar{S}_z} \right), \end{aligned} \quad (8)$$

where the approximation made is based upon the assumptions that  $\Theta'_z/\bar{\Theta}_z \ll 1$  and  $S'_z/\bar{S}_z \ll 1$ . It is important to notice that the background density ratio  $\bar{R}_\rho(z)$  is also depth dependent in the above. We may then proceed to derive the expression for  $\partial R_\rho/\partial z$  again to first order in the perturbations:

$$\frac{\partial R_\rho}{\partial z} \approx \frac{\partial \bar{R}_\rho}{\partial z} \left( 1 + \frac{\Theta'_z}{\bar{\Theta}_z} - \frac{S'_z}{\bar{S}_z} \right) + \bar{R}_\rho \left( \frac{\Theta'_{zz}\bar{\Theta}_z - \bar{\Theta}_{zz}\Theta'_z}{\bar{\Theta}_z^2} - \frac{S'_{zz}\bar{S}_z - \bar{S}_{zz}S'_z}{\bar{S}_z^2} \right). \quad (9)$$

The above expressions (8) and (9) allow us to expand the governing equation (2) to first order in the perturbation fields  $\Theta'$  and  $S'$  (using the temperature equation as an example) to obtain

$$\begin{aligned} \frac{\partial \bar{\Theta}}{\partial t} + \frac{\partial \Theta'}{\partial t} &= \frac{\partial \text{Nu}}{\partial z} (\bar{\Theta}_z + \Theta'_z) + \text{Nu}|_{R_\rho} (\bar{\Theta}_{zz} + \Theta'_{zz}) \\ &\approx \frac{\partial \text{Nu}}{\partial R_\rho} \Big|_{\bar{R}_\rho} \frac{\partial R_\rho}{\partial z} (\bar{\Theta}_z + \Theta'_z) + \left[ \text{Nu}|_{\bar{R}_\rho} + \frac{\partial \text{Nu}}{\partial R_\rho} \Big|_{\bar{R}_\rho} (R_\rho - \bar{R}_\rho) \right] (\bar{\Theta}_{zz} + \Theta'_{zz}) \\ &\approx \frac{\partial \text{Nu}}{\partial R_\rho} \Big|_{\bar{R}_\rho} \left[ \frac{\partial \bar{R}_\rho}{\partial z} \left( 1 + \frac{\Theta'_z}{\bar{\Theta}_z} - \frac{S'_z}{\bar{S}_z} \right) + \bar{R}_\rho \left( \frac{\Theta'_{zz}\bar{\Theta}_z - \bar{\Theta}_{zz}\Theta'_z}{\bar{\Theta}_z^2} - \frac{S'_{zz}\bar{S}_z - \bar{S}_{zz}S'_z}{\bar{S}_z^2} \right) \right] (\bar{\Theta}_z + \Theta'_z) \\ &\quad + \text{Nu}|_{\bar{R}_\rho} (\bar{\Theta}_{zz} + \Theta'_{zz}) + \frac{\partial \text{Nu}}{\partial R_\rho} \Big|_{\bar{R}_\rho} \bar{R}_\rho \left( \frac{\Theta'_z}{\bar{\Theta}_z} - \frac{S'_z}{\bar{S}_z} \right) (\bar{\Theta}_{zz} + \Theta'_{zz}) \end{aligned} \quad (10)$$

in which the first approximation is made by employing linear expansions of Nu and  $\frac{\partial \text{Nu}}{\partial R_\rho}$  as a function of  $R_\rho$ , and the second approximation is made by substituting the expressions (8) and (9). By balancing terms of the same order in the perturbations in (10), at zeroth order the following balance condition must hold:

$$\frac{\partial \bar{\Theta}}{\partial t} = \frac{\partial \text{Nu}}{\partial R_\rho} \Big|_{\bar{R}_\rho} \frac{\partial \bar{R}_\rho}{\partial z} \bar{\Theta}_z + \text{Nu} \Big|_{\bar{R}_\rho} \bar{\Theta}_{zz}. \quad (11)$$

At first order from (10), the balance is the following for the evolution of the temperature perturbation (that for the evolution of the salinity perturbation is simply stated following the result for the



temperature perturbation) as

$$\begin{aligned}
 \frac{\partial \Theta'}{\partial t} &\approx \frac{\partial \text{Nu}}{\partial R_\rho} \left[ \frac{\partial \bar{R}_\rho}{\partial z} \Theta'_z + \frac{\partial \bar{R}_\rho}{\partial z} \left( \frac{\Theta'_z}{\bar{\Theta}_z} - \frac{S'_z}{\bar{S}_z} \right) \bar{\Theta}_z + \bar{R}_\rho \left( \frac{\Theta'_{zz} \bar{\Theta}_z - \bar{\Theta}_{zz} \Theta'_z}{\bar{\Theta}_z^2} - \frac{S'_{zz} \bar{S}_z - \bar{S}_{zz} S'_z}{\bar{S}_z^2} \right) \bar{\Theta}_z \right] \\
 &\quad + \text{Nu} \Big|_{\bar{R}_\rho} \Theta'_{zz} + \frac{\partial \text{Nu}}{\partial R_\rho} \Big|_{\bar{R}_\rho} \bar{R}_\rho \left( \frac{\Theta'_z}{\bar{\Theta}_z} - \frac{S'_z}{\bar{S}_z} \right) \bar{\Theta}_{zz} \\
 &= \frac{\partial \text{Nu}}{\partial R_\rho} \left[ 2 \frac{\partial \bar{R}_\rho}{\partial z} \right] \Theta'_z + \left[ \frac{\partial \text{Nu}}{\partial R_\rho} \bar{R}_\rho + \text{Nu} \right] \Theta'_{zz} \\
 &\quad + \frac{\partial \text{Nu}}{\partial R_\rho} \left[ -\frac{\partial \bar{R}_\rho}{\partial z} \bar{R}_\rho + \bar{R}_\rho^2 \left( \frac{\bar{S}_{zz}}{\bar{S}_z} - \frac{\bar{\Theta}_{zz}}{\bar{\Theta}_z} \right) \right] S'_z - \frac{\partial \text{Nu}}{\partial R_\rho} \bar{R}_\rho^2 S'_{zz} \\
 &= 2A_2 A_3 \Theta'_z + (A_2 + \text{Nu}) \Theta'_{zz} + A_2 \bar{R}_\rho (-A_3 + A_S - A_\Theta) S'_z - A_2 \bar{R}_\rho S'_{zz} \\
 \frac{\partial S'}{\partial t} &\approx \frac{A'_2}{\bar{R}_\rho} [A_3 + A_S - A_\Theta] \Theta'_z + \frac{A'_2}{\bar{R}_\rho} \Theta'_{zz} + [\text{Nu}_S - A'_2] S'_{zz}, \tag{12}
 \end{aligned}$$

in which  $A_1 = \frac{\partial \gamma^{-1}}{\partial R_\rho} \Big|_{\bar{R}_\rho} \bar{R}_\rho$  and  $A_2 = \frac{\partial \text{Nu}}{\partial R_\rho} \Big|_{\bar{R}_\rho} \bar{R}_\rho$  are defined in a similar way as in the last subsection, and we have defined the additional parameters  $A_3 = \frac{1}{\bar{R}_\rho} \frac{\partial \bar{R}_\rho}{\partial z}$ ,  $A_\Theta = \frac{\bar{\Theta}_{zz}}{\bar{\Theta}_z}$ , and  $A_S = \frac{\bar{S}_{zz}}{\bar{S}_z}$  to represent the depth variations of  $\bar{\Theta}_z$  and  $\bar{S}_z$ .  $\text{Nu}_S$  is the salinity Nusselt number and  $A'_2 = \frac{\partial \text{Nu}_S}{\partial R_\rho} \Big|_{\bar{R}_\rho} \bar{R}_\rho$ . It should be clear that  $\text{Nu}_S$  and  $A'_2$  are related to other variables through  $\text{Nu}_S = \text{Nu} R_\rho \gamma^{-1}$  and  $A'_2 = (A_2 \gamma^{-1} + \text{Nu} \gamma^{-1} + A_1 \text{Nu}) R_\rho$  and have been introduced solely to simplify (12).

While the existence of the new terms  $A_3$ ,  $A_\Theta$ , and  $A_S$  makes the forms of (12) more complicated than (6), it is important to notice that in the special case of  $A_3 = 0$  and  $A_\Theta = A_S$ , all of these extra terms that involve  $A_3$ ,  $A_\Theta$ , and  $A_S$  are eliminated from (12) and (12) exactly returns to (6). In fact, for the typical staircases (see Fig. 1 of Ref. [4], for example), the background temperature profile and salinity profile share almost the same shape, resulting in both a depth-independent background  $\bar{R}_\rho$  (which leads to  $A_3 \approx 0$ ) and negligible differences between  $A_\Theta$  and  $A_S$  (which means  $A_\Theta \approx A_S$ ). In other words, if we apply our linear stability analysis to a system that mimics the observational data, the basic equations that are subject to linear stability analysis will remain the same as in the case of the homogeneous system. Thus, the same  $\gamma$  criterion will be governing the linear stability of the system, as we discussed in the last section. The analysis for the case in which the conditions ( $A_3 = 0$ ,  $A_\Theta = A_S$ ) are not satisfied is not relevant to the following discussion but is discussed explicitly in Appendix A of this paper.

### C. Remedy for the ultraviolet catastrophe in $\gamma$ instability theories

In the past two subsections, we have both reviewed the original  $\gamma$  instability analysis and shown that the alternative formulas for  $\gamma$  instability in a vertically inhomogeneous system remain the same as in the homogeneous case in the physically relevant regime. When the  $\gamma$  criterion is satisfied, the growth rate in both of these systems will be determined by (7) and can easily be shown to be proportional to the square of the vertical wave number  $k$ . This ultraviolet catastrophe reveals what might be a fatal flaw in this theory which prevents us from inferring the fastest growing scale at which layering would be expected to form. This problem originates from the assumption that the mean field equations described in (2) are valid at any length scale, while in reality the mean field equations are only accurate on scales that are at least an order of magnitude larger than the salt-finger widths [12]. This flaw of the theory has recently been resolved in the multiscale model developed in [26], which carefully incorporates the interaction between different scales into the theory. These interactions have been shown to damp the high-order perturbations in the mean-field equation and thereby lead to a well-defined most quickly growing mode.



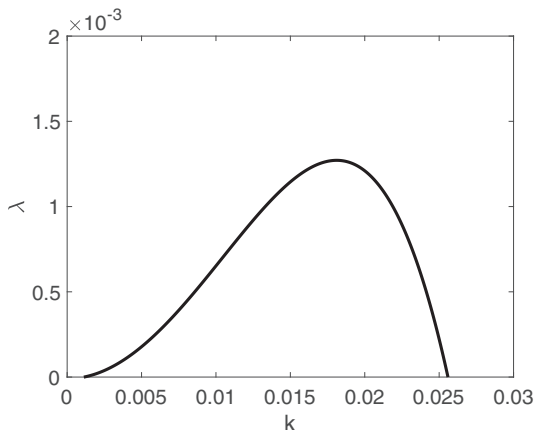


FIG. 3. The growth rate  $\lambda$  plotted as a function of vertical wave number  $k$  in the case of  $R_\rho = 1.5$ ,  $\text{Pr} = 7$ ,  $\tau = 0.01$ , and  $\mu = 1.19 \times 10^4$ . The fastest growth rate is obtained at the value of  $k_{\text{max}} = 0.0181$ .

In this work, we will employ a much simpler remedy for the ultraviolet catastrophe, namely by introducing a hyperdiffusion term in both the temperature and salinity diffusion equations to damp high-order modes as

$$\begin{aligned} \frac{\partial \Theta}{\partial t} &= -\frac{\partial}{\partial z} F_\Theta - \mu \frac{\partial^4}{\partial z^4} \Theta, \\ \frac{\partial S}{\partial t} &= -\frac{\partial}{\partial z} F_S - \mu \frac{\partial^4}{\partial z^4} S, \end{aligned} \quad (13)$$

where  $\mu$  is the hyperdiffusivity which has physical units of  $m^4/s$ . This term has also been introduced in previous mean-field model simulations in Refs. [15] and [16] in which its value can only be estimated crudely from the initially formed staircases in DNS. Since the most quickly growing wavelength has already been calibrated in the multiscale theory, we can adjust  $\mu$  to a value so that the most quickly growing wavelength reaches the same value as predicted by the multiscale theory. We can then solve the modified eigenvalue problem [with the hyperdiffusion terms added to (12)] to calculate the growth rate. For the case of  $R_\rho = 1.5$ ,  $\text{Pr} = 7$ , and  $\tau = 0.01$ , we find that  $\mu = 1.19 \times 10^4$  leads to a value of the most quickly growing vertical wave number of  $k_{\text{max}} = 0.0181$ , which is consistent with the prediction of the multiscale theory in Ref. [26]. Specifically, the growth rate increases with  $k$  for  $k < k_{\text{max}}$  but decreases when  $k > k_{\text{max}}$ , reaching the maximum value of  $\lambda_{\text{max}} = 0.0013$  at  $k_{\text{max}}$ , as shown in Fig. 3. The growth rate of the most quickly growing mode and the most quickly growing wave number will be tested in the fully nonlinear model simulation for the same nondimensional parameters as will be discussed in the next section.

#### IV. PARAMETERIZED MEAN FIELD SIMULATIONS FOR THE SALT-FINGERING INTERFACE MODEL

##### A. Model settings

While the influence of depth variations of temperature and salinity gradients have already been well understood in the linear regime, it is not yet clear how the inhomogeneity will affect the evolution of the system once the perturbation enters the nonlinear regime. To this end, we will perform numerical simulations for a 1D mean field model whose evolution is fully governed by the parametrized diapycnal diffusivities for temperature and salinity.

The system is initialized with hyperbolic-tangent profiles for both temperature and salinity, namely,

$$\begin{aligned}\Theta_0(z) &= \Delta\Theta \tanh(z/h), \\ S_0(z) &= \Delta S \tanh(z/h).\end{aligned}\tag{14}$$

The vertical domain is chosen to have equal heights and depths from the centerline  $-H \leq z \leq H$ , where the vertical domain half-height  $H$  is chosen to be 8160 and the interface depth  $h = 2/5H = 3264$ . In dimensional units, this corresponds to  $H \approx 75$  m and  $h \approx 30$  m. We have designed these initial profiles for temperature and salinity to resemble the shape and scale of background temperature and salinity profiles in the main thermocline of the tropical ocean.

The evolution of this initial profile is then governed by the following set of equations:

$$\begin{aligned}\frac{\partial \Theta}{\partial t} &= -\frac{\partial}{\partial z} F_\Theta - \mu \frac{\partial^4}{\partial z^4} \Theta + R_\Theta, \\ \frac{\partial S}{\partial t} &= -\frac{\partial}{\partial z} F_S - \mu \frac{\partial^4}{\partial z^4} S + R_S,\end{aligned}\tag{15}$$

in which  $R_\Theta$  and  $R_S$  are defined as

$$\begin{aligned}R_\Theta(z) &= -R_0(\Theta(z, t) - \Theta_0(z)), \\ R_S(z) &= -R_0(S(z, t) - S_0(z)),\end{aligned}\tag{16}$$

where  $R_0$  has the dimension of inverse of time. These new terms  $R_\Theta$  and  $R_S$  are defined to represent a restoring force that we will employ in order to ensure that the model evolves in such a way as to retain the shape of the initial background temperature and salinity profiles; otherwise, the steep gradients of temperature and salinity at the center of the domain will cause both heat and salt to be constantly transferred from the upper domain to the lower domain in such a way as to erode the thermocline. By adding these restoring forces, we can mimic the physical circumstances that ensure that the staircase will form and thereafter be trapped in the stable main thermocline of the oceans, which our background profiles are intended to model. As discussed in detail in Appendix B, these restoring forces can be viewed as representing the influence of downwelling associated with Ekman pumping from the surface mixed layer as well as the upwelling of deep water in the mid-latitude ocean. The value of  $R_0$  must be chosen so that the restoring force is strong enough to balance the overall vertical diffusion of the system but meanwhile weak enough to avoid influencing the growth of the  $\gamma$  instability derived perturbations. A value of  $R_0 = 10^{-5}$  has been found by experiment to satisfy these requirements, as will be further discussed in Appendix B.

In (15),  $F_\Theta$  and  $F_S$  are parametrized by (3) when  $R_\rho > 1$ . On the other hand, we assume a large constant ( $K_c = 2000\kappa_\theta$ ) for diapycnal diffusivity for both temperature and salinity when density inversions occur in the water columns ( $R_\rho < 1$ ), a method that has been employed to represent the convective mixing in the kappa-profile parametrization (KPP) scheme ([27]; see also Ref. [28] for a recent discussion of the importance of this scheme for the parametrization of diapycnal diffusivity in the context of an important problem in large-scale ocean dynamics).

We initialize our nonlinear simulations by adding white noise of magnitude  $10^{-5} \Delta\Theta$  ( $10^{-5} \Delta S$ ) to the initial profiles of both temperature and salinity. No flux boundary conditions will be applied for  $\Theta(z, t)$  and  $S(z, t)$  at the boundaries  $z = -H$  and  $z = H$ . The system (15) is then integrated using a finite difference scheme composed of 1632 grid points.

## B. Simulation results

We will first proceed to test the linear stability analysis described at the end of the last section. It should be noticed, however, that the no-flux boundary conditions and the restoring forces  $R_\Theta$  and  $R_S$  will both influence the linear stability analysis process described above; however, both of these influences will be negligible so that we can safely retain the result for the linear stability analysis discussed previously. Once the no-flux boundary condition is applied in the finite domain  $(-H, H)$ , the most quickly growing vertical wave number  $k$  can no longer assume arbitrary values.

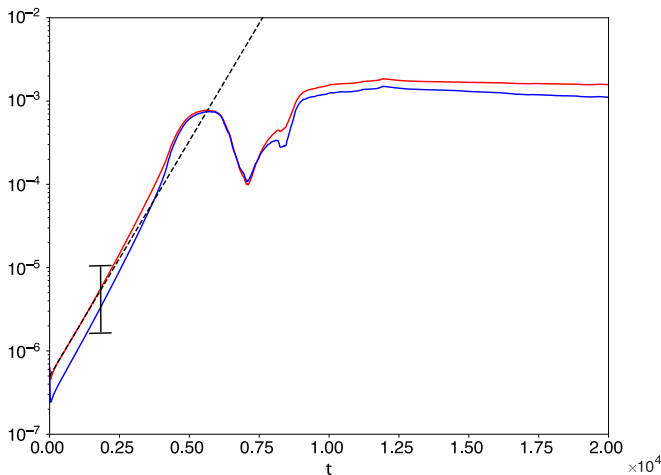


FIG. 4. The evolution of the most quickly growing mode of temperature (red solid curve) and salinity (blue solid curve), compared with the exponential growth (dashed curve) predicted from the linear stability analysis described in the last section. The growth rate from linear stability analysis precisely predicts the growth of the most quickly growing mode prior to approximately  $t = 2000$ .

In fact, it can only assume a series of specific values of  $k_n = n\pi/H$  so that the first derivatives of perturbations can vanish at the boundaries  $z = -H$  and  $z = H$ . However, since  $H = 8160$  is large enough, the spectrum of  $k_n$  is sufficiently close to continuous so that the fastest growing wave number  $k_{\max} = 0.0181$  can be found with a close value of  $k_{47} = 47\pi/H = 0.0181$  in the spectrum. This also suggests that a staircase with 47 steps will form initially at the wavelength of approximately 347. The additional term that is related to the restoring force in the matrix eigenvalue problem is proportional to an identity matrix with the coefficient  $-R_0$ , which has no effect on the eigenfunctions but only acts to lower the corresponding eigenvalues to a finite value of  $R_0$ . As we have chosen  $R_0 = 10^{-5}$  so that it is two orders of magnitude smaller than the highest growth rate  $\lambda_{\max} = 1.3 \times 10^{-3}$ , we can safely ignore its influence on the exponential growth of initial perturbations. Figure 4 shows the evolution of the most quickly growing mode for both temperature and salinity from  $t = 0$ –20 000. It is clear that our linear stability analysis result precisely predicts the dynamics of the system in the initial stage of exponential growth between  $t = 0$ –2000, but after  $t = 2000$  the growth of the perturbation starts to deviate from the predicted trend, as  $\bar{R}_\rho$  begins to increase at the center and decrease on the flanks so as to deviate from the initial constant value. We will discuss this trend in detail in the next subsection.

Figure 5 presents several snapshots of the temperature profiles after the system enters the non-linear regime. The staircase first forms in the low-gradient region near the edges of the hyperbolic tangent interface [Fig. 5(b)] and then gradually extends into the high-gradient region at the center of the interface [Fig. 5(c)]. At  $t = 10\,000$ , the staircase structure has developed throughout the domain and the steps that form at different vertical positions are all of very similar size. This initially formed staircase is characterized by an interstep wave number of  $k_{\max}$  that is predicted accurately on the basis of the linear stability analysis.

The initially formed staircase then undergoes a series of merging events as shown in Figs. 5(e)–5(h). These merging events occur through the erosion of some interfaces together with the strengthening of neighboring interfaces, exemplified by the evolution of the single staircase shown in the boxes in Figs. 5(e)–5(g). This merging process follows the B merger mechanism as initially proposed in Ref. [15]. The layer merging events once more begin in regions of low gradient. At  $t = 16\,000$ , there has already been very apparent layer merging events in the low-gradient region near the edges of the interface. However, the steps in the staircase in the high-gradient region

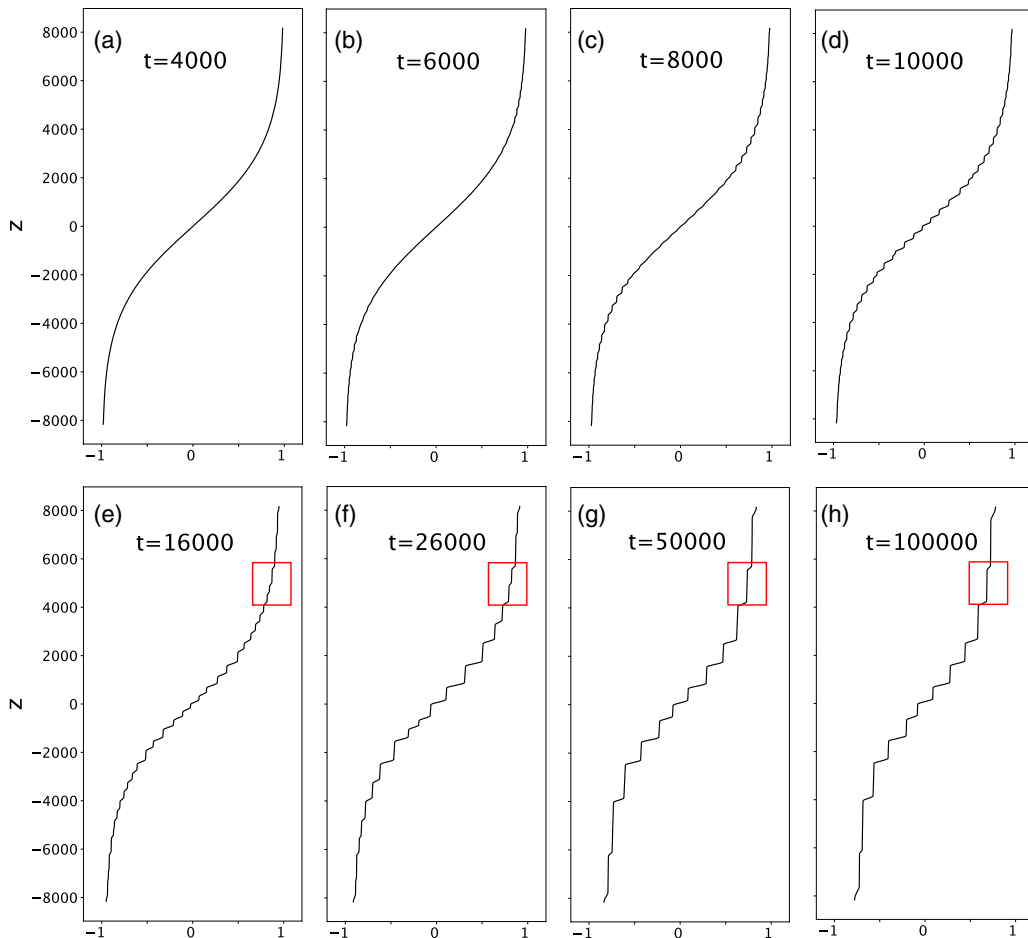


FIG. 5. The evolution of the temperature profile  $\Theta(z)$  as a function of nondimensional time. The figures on the top row illustrate the formation of the initial staircase while the figures on the bottom row depict a succession of layer merging events.

are observed to retain the initial step sizes. The merging of the steps in the high-gradient region only become apparent at approximately  $t = 26\,000$  [Fig. 5(f)]. During this period, the steps in the high-gradient region have already merged into larger steps. The merging of steps in all vertical regions is eventually complete by approximately  $t = 50\,000$  [Fig. 5(g)] and the ensuing evolution of the system does not change the step sizes further [as demonstrated by Fig. 5(h)]. Although the staircase ceases to evolve due to the continuing operation of the merging instability at approximately  $t = 50\,000$ , the system continues to evolve until  $t = 80\,000$  (not shown), after which the system remains almost in the same state. Thus, our system produces a situation that very closely resembles the oceanographic observations mentioned above: The staircase step sizes are always higher in the low-gradient region compared to those in the high-gradient region, in both the process of evolution as well as in the equilibrium state of the system.

### C. Analysis of the simulation results

Before we are in a position to discuss the connection between this simulation and the staircases observed in the real oceans, we must first answer three questions related to the above discussed simulation: (1) Why does the staircase structure form more quickly in the low-gradient region

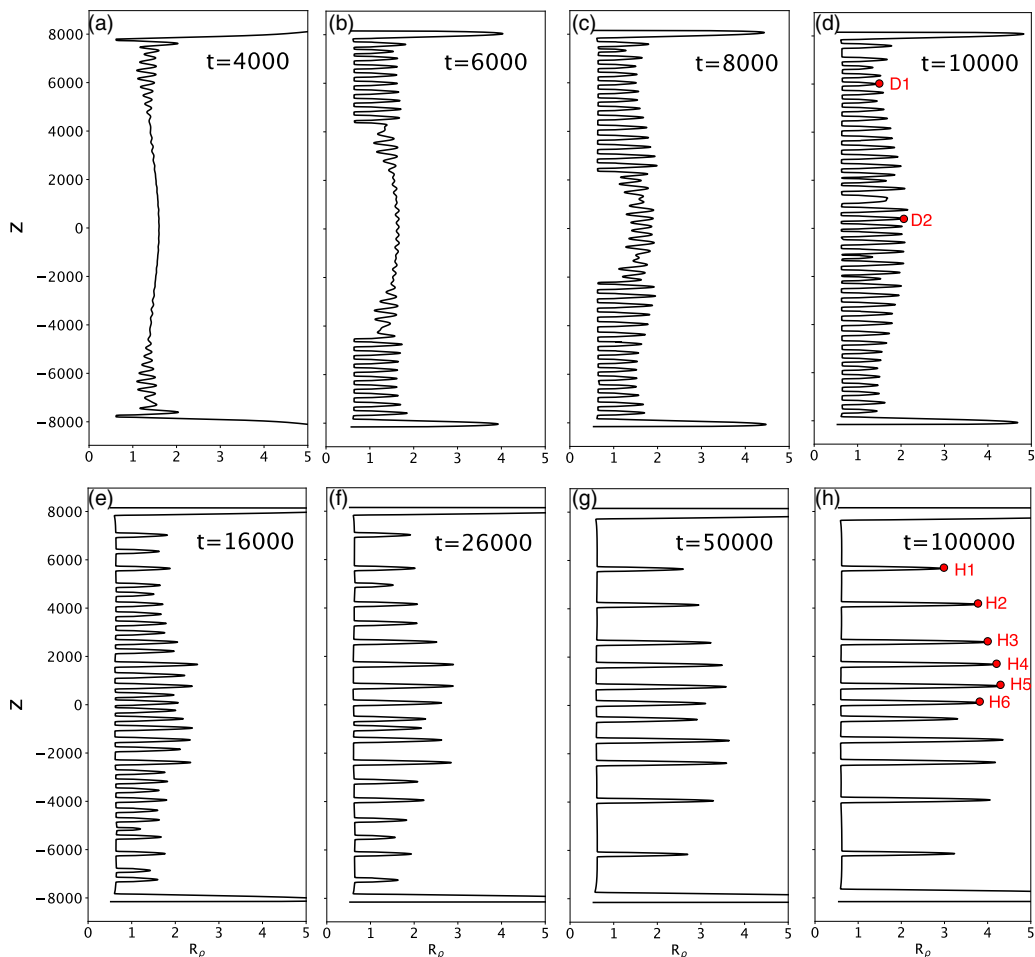


FIG. 6. The evolution of the  $R_\rho(z)$  as a function of nondimensional time in the stage of the formation of the initial staircase. The regions of  $R_\rho < 1$  corresponding to the homogenous layers where deep convection occurs and peaks in  $R_\rho$  suggest the positions of interfaces. We specifically label several specific interfaces as  $D1$ ,  $D2$ , and  $H1$ – $H6$  as an aid for the analysis in what follows.

compared with the high-gradient region? (2) Why do adjacent stairs in the staircase merge more quickly in the low-gradient region than in the high-gradient region? (3) Why does the system equilibrate into a state in which step sizes are generally larger in the low-gradient region?

To answer these questions, we plot on Figs. 6(a)–6(h) the depth dependence of the governing parameter  $R_\rho$  for each of the eight time slices at which Figs. 5(a)–5(h) are plotted. The regions in which  $R_\rho < 1$  (equivalent to  $\partial\rho/\partial z > 0$ ) suggests the formation of a convectively mixed layer in the environment that is gravitationally unstable. [The  $R_\rho$  in convectively mixed layers, which equals the flux ratio in interfaces, has to fall into a narrow parameter range (0.5–0.65) in order to be consistent with the interface flux ratio which is bounded by the flux law in (4).] On the other hand, the large peaks of  $R_\rho$  between two convectively mixed layers determine the positions of the interfaces. Thus, Figs. 6(a)–6(h) provide a clear picture of the evolutionary trajectory of the staircase. The heights in the convectively mixed layers  $H_L$  generally increase with time, caused by the merging of neighboring steps in the staircase. The heights of the interfaces, on the other hand,

are determined by the strength of the hyperdiffusivity we have employed [15] and is fixed to the value of approximately 200 throughout the evolution process.

In answering the previously posed questions, we will focus first upon the reason the first formation of layers occurs in the low-gradient regions, although this might be seen as counterintuitive since our linear stability analysis has demonstrated that the most quickly growing mode has equal magnitude in the low-gradient region and the high-gradient region. Thus, it is natural for us to expect that the most quickly growing perturbations  $\Theta'$  and  $S'$  should grow equally quickly in these two regions (in the linear regime). However, it is important to recognize that the governing nondimensional parameter  $R_\rho$  depends on the linear perturbations through the relationship  $R_\rho(z) = \bar{R}_\rho(1 + \Theta'_z/\bar{\Theta}_z - S'_z/\bar{S}_z)$  [derived previously in (8)]. Even though  $\Theta'_z$  and  $S'_z$  have the same magnitude in the low-gradient region and the high-gradient region in the most quickly growing mode, their influence on  $R_\rho$  is significantly amplified in the low-gradient regions where the denominators  $\bar{\Theta}_z$  and  $\bar{S}_z$  are small, compared with high-gradient region. This can be confirmed in the  $R_\rho(z)$  profile shown in Fig. 6(a):  $R_\rho(z)$  has a vertical oscillation of larger magnitude in the low-gradient regions near the edges of the model thermocline than in the high-gradient region at the most quickly growing wave number  $k_{\max}$ . Since a convectively mixed layer forms whenever  $R_\rho$  oscillates so as to reach a value that is smaller than 1, the layered structure is destined to form more quickly in the low-gradient region where oscillations in  $R_\rho$  are strong.

The explanation for quicker merging in the low-gradient region, on the other hand, relies on the B-merger mechanism as proposed in Ref. [17]. We will briefly review the key conclusion here in order to make further comparisons. In Ref. [15], the author introduced the following variables to represent the relative amplitude of merging perturbations:

$$\begin{aligned} A &= \frac{\Delta\Theta_2 - \Delta\Theta_1}{\Delta\Theta_I}, \\ B &= \frac{\Delta S_2 - \Delta S_1}{\Delta S_I}, \end{aligned} \quad (17)$$

where  $\Delta\Theta_2$ ,  $\Delta S_2$  ( $\Delta\Theta_1$ ,  $\Delta S_1$ ) denote the temperature and salinity jumps across the interfaces that are about to be strengthened (weakened) by the layer merging instability, and  $\Delta\Theta_I$  and  $\Delta S_I$  represent the temperature and salinity jumps across the interfaces before the development of the merging instability. Therefore,  $A = B = 0$  before merging and the growth of  $A$  and  $B$  is suggestive of the gradual merging of these two neighboring interfaces. ( $A$ ,  $B$ ) were further expanded into normal modes  $(A_0, B_0)\exp(\lambda t)$  and the growth rate  $\lambda$  has been shown to obey the following quadratic equation [see Eq. (A3) of Ref. [15] where the parameters  $a = 0$ ,  $b = 1$  have been chosen to be consistent with the flux laws being employed in the present paper]:

$$\lambda^2 + \frac{4}{H_L} \left[ C(R_I) + D_2 - \frac{R_I D_2}{\gamma(R_I)} - D_1 C(R_I) R_I \right] \lambda - \frac{16}{H_L^2} C^2(R_I) D_1 R_I = 0, \quad (18)$$

where  $H_I$  and  $H_L$  represent the heights of staircase interfaces and convectively mixed layers, respectively.  $R_I = \Delta\Theta_I/\Delta S_I$  is the density ratio at the interfaces.  $C(R_I)$ ,  $D_1$ , and  $D_2$  are defined to depend solely on density ratio  $R_I$ , namely:

$$\begin{aligned} C(R_\rho) &= \frac{\text{Nu}(R_\rho)}{H_I}, \\ D_1 &= \left. \frac{\partial(1/\gamma)}{\partial R_\rho} \right|_{R_\rho=R_I} R_I, \\ D_2 &= \left. \frac{\partial C}{\partial R_\rho} \right|_{R_\rho=R_I} R_I. \end{aligned} \quad (19)$$

In the above formulas, the growth rate  $\lambda$  is only determined by  $H_I$ ,  $H_L$ , and  $R_I$  since the other free parameters  $D_1$  and  $K_\Theta$  are fixed once the parametrization scheme for  $\text{Nu}(R_\rho)$  and  $\gamma(R_\rho)$  are

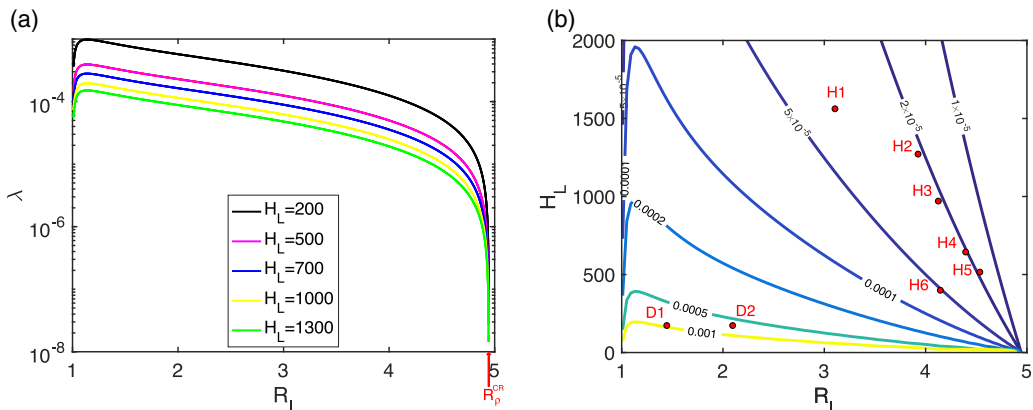


FIG. 7. (a) The growth rate of layer merging instability as a function of interface density ratio  $R_I$  at different  $H_L$  calculated from (18). The growth rate reduces to 0 at the critical value  $R_{\rho}^{cr}$ . (b) Contour plot of the stability diagram plotted in the 2D parameter space of  $(R_I, H_L)$ . The interfaces labeled in Fig. 6 are represented by red dots in the 2D parameter space.

determined by (4). By taking  $H_I = 200$ , the functional relationship  $\lambda(R_I)$  at different  $H_L$  may be evaluated for our system and this is shown in Fig. 7(a). The growth rate has a negative dependence with respect to the interface density ratio  $R_I$  at all values of  $H_L$  as long as  $R_I > 1.14$ .

At the stage of the system displayed in Fig. 6(d), the layer depth  $H_L$  has the same value of approximately 150 in all depth ranges, as determined by the fastest growing mode from the linear stability analysis. The interface  $R_I$ , however, generally has a much smaller value (near 1.5) in the low-gradient region compared with the high-gradient region (where it is near 2). Based on the functional relationship  $\lambda(R_I)$  shown in Fig. 7(a), we can conclude that the layer merging instability has a much higher growth rate in the low-gradient region compared with the high-gradient region. The reason for a higher  $R_I$  in the high-gradient region can be traced to a stage prior to the formation of layers [Fig. 6(a)], in which it is clear that the density ratio  $R_{\rho}$  has a higher value in the center of the domain than near the edges of the model thermocline. This variation of  $R_{\rho}(z)$  is induced by the imbalance in the strength of the fluxes at different vertical positions as discussed and explained in Ref. [24], in which DNS simulations were performed using the same model. Briefly put, in the system that has different gradients at different vertical positions, the vertical fluxes (either heat flux or salt flux) have to reach a coarse balance in neighboring regions to remain in a quasiequilibrium state (otherwise, the divergence and convergence of fluxes will quickly adjust the local temperature and salinity in order to satisfy this condition). The coarse balance can only be approached if the relatively higher gradient region has a relatively smaller diapycnal diffusivity, which can only obtain at a relatively higher value of  $R_{\rho}$  based on the flux laws shown in Fig. 2.

The final equilibrium of the system can also be explained by referring to the layer merging instability presented in (18). However, instead of studying the growth rate of layer merging instability for early-stage interfaces [exemplified by D1 and D2 in Fig. 6(d)], we need rather to study the growth rate of layer merging instability in the equilibrium state: The represented interfaces have been marked as H1–H6 in Fig. 6(h), which range from the low-gradient region to the high-gradient region. The interface density ratio  $R_I$  as well as layer height  $H_L$  (calculated as the average height of two neighboring layers) for these six interfaces are marked in the stability diagram for layer-merging instability in Fig. 7(b). For interfaces H2, H3, H4, and H5, the layer merging instability has a finite growth rate of approximately  $2 \times 10^{-5}$  and for H1 and H6 the growth rates are higher but remain constrained close to order  $10^{-5}$ . It is then a natural question as to why the layers cease merging in the simulation while there is still finite merging growth rate at these interfaces? In fact, in the original theory of Ref. [15] the author made the assumption that the layers will keep merging until



the merging growth rate goes to 0 at the critical density ratio  $R_\rho^{cr} = 4.95$  shown in Fig. 7(a). This leads the author to the conclusion that all interface density ratios  $R_\rho$  will reach the value of  $R_\rho^{cr}$  in the equilibrium state.

This assumption is violated in our system due to the action of the restoring force employed in the simulation to prevent complete destruction of the model thermocline: The restoring force in (B3), which serves to “trap” the staircase on the model thermocline, will act to suppress any form of instability by appearing as a negative constant term in the eigenvalue matrix. In this special case of layer merging instability, the variation of the temperature in convectively mixed layers will lead to the same degree of temperature (same argument applies for salinity equation) change in both nearby interfaces  $\Delta\Theta_2$  and  $\Delta\Theta_1$  of the opposite sign, and thus the change of  $A = (\Delta\Theta_2 - \Delta\Theta_1)/\Delta\Theta_l$  will be suppressed by the restoring force with twice the strength. This leads to the conclusion that the true growth rate of merging instability in the presence of the restoring force must be reduced by a constant that equals  $2R_0 = 2 \times 10^{-5}$ . In other words, the merging event can only occur if the growth rate of merging instability exceeds  $2R_0 = 2 \times 10^{-5}$ . This explains why most of the interfaces characteristic of the equilibrium state live near the contour line characterized by  $\lambda = 2 \times 10^{-5}$  in the stability diagram. The outliers of  $H1$  and  $H6$  should be expected to go through further merging events since their growth rate exceeds  $2R_0$ , but such potential merging events will only happen after a nondimensional simulation time of order  $10^5$ .

As discussed above, the equilibrium state of our model is achieved when the restoring force implemented in our system balances the growth of the layer merging instability. However, the value of the restoring parameter  $R_0$  is still somewhat arbitrarily selected in our model and we have been able to relate it only qualitatively to the upwelling and downwelling processes that serve to maintain the existence of the thermocline on which such staircases are observed to be trapped (see our further discussion in Appendix B). As a result, the relationship between the equilibrium state of our model staircases and those of the real ocean remains somewhat unclear. Despite this caveat concerning the equilibrium states of our model staircases, the following systematic relationship is found to hold for any value of  $R_0$ , namely that the  $H_L - R_l$  slope is always negative on the equal-growth-rate contour line as illustrated on Fig. 7(b). As  $R_l$  has been shown to be always higher in the high-gradient region, the equilibrium  $H_L$  is naturally lower there. In this way, we have answered the third question proposed at the beginning of this subsection.

To summarize, we have been able to explain three important correlations that are observed to be characteristic of our mean-field model simulations of salt fingering staircases, all related to the comparisons between high-gradient regions and low-gradient regions. First, the layered structure forms more quickly in the low-gradient region because the perturbation of the density ratio  $R'_\rho$  is more sensitive to  $\Theta'$  and  $S'$  in the low-gradient regions. Second, the layers merge more quickly in the low-gradient region because the interface density ratios  $R_l$  are generally lower there, which leads to a higher growth rate of layer merging instability based on the theory of Ref. [15]. The lower  $R_l$  in the low-gradient regions derives from a lower background density ratio  $\bar{R}_\rho$  there, which is caused by the tendency to realize a coarse balance of fluxes in regions of different gradients. Finally, the layers equilibrate to a state such that the growth-rate of layer merging instability is balanced by the restoring force that has been introduced in our system to restrain the overall diffusion on a long timescale. In this equilibrium state, the step sizes  $H_L$  are negatively correlated with  $R_l$  as characterized by the  $2R_0$  contour line in 7(b), and thus the step sizes are generally higher in the lower gradient region where  $R_l$  is lower.

In our discussions above, we have illustrated the mechanism that leads to systematically higher step sizes in the low gradient region by dynamically simulating the formation and evolution of the thermohaline staircases in an inhomogeneous system. However, it is also worthwhile for us to re-examine this phenomenon from a static perspective. In fact, the layering height for temperature (same argument applies for the salinity field) in the layering state can be well approximated by the relation  $H_L = \Delta\Theta/\bar{\Theta}_z$ , where  $\bar{\Theta}_z$  is the background temperature gradient. It will be immediately recognized from this expression that step sizes  $H_L$  tend to be larger in lower gradient region, as long as  $\Delta\Theta$  has similar values for different interfaces. Unfortunately, this assumption does not

hold. In both our numerical simulations (shown in Fig. 5) as well as oceanographic observations (e.g., Refs. [2,4]),  $\Delta\Theta$  is found to be much smaller in the low-gradient region than in the high-gradient region. This is a consequence of the (quasi) flux balance that needs to be reached between different interfaces: The high-gradient region has smaller diapycnal diffusivities at the interfaces (induced by higher  $R_I$ ) and thus it needs to have higher  $\Delta\Theta$  to support the required flux. As a result, although background gradients tend to negatively influence the value of layer depth  $H_L$ , a complete explanation of the differences in  $H_L$  must take the differences of  $R_I$  into account, as we have demonstrated above.

#### D. Comparison with oceanographic observations

As we have discussed in the introduction, it has been a routinely observed characteristic of observational data sets that the thermohaline staircases have larger step sizes in a low-gradient region than in a high-gradient region. In this subsection, our intention is to explain this observation utilizing the results obtained in the simulation described above.

Among all of the different observations of staircases in the ocean, the best example that clearly shows the layer merging events comes from the historical record of salt-fingering thermohaline staircases in the Tyrrhenian Basin. Staircase data in the central part of the Tyrrhenian Sea basin has been summarized and studied from 1973 to 1992 in Ref. [2], from 2007 to 2009 in Ref. [29], and most recently from 2003 to 2016 in Ref. [30]. The layer-merging events are mainly captured in the work of Ref. [2], where the temperature and salinity data for depth range 600–1600 m taken in years 1973, 1979, 1987, and 1992 are specifically plotted and compared in Fig. 11(a) of Ref. [2]. The layers display consecutive merging through these years: The approximately 10-step staircase in year 1973 evolves to an approximately six-step staircase in year 1979, and further evolves to an (approximately) three-step structure in years 1987 and 1992. All of the staircase data in these four years display significantly higher step sizes in the low-gradient region (850–1400 m) than in the high-gradient region (650–850 m). This merging pattern greatly resembles the temperature profile evolution in our simulation shown in Figs. 5(e)–5(h): The layered state is a more unstable state in the low-gradient region compared to the high-gradient region and layers in the lower gradient region merge more efficiently during the entire layer merging process. Since we have already understood that the layers merge more quickly in the low-gradient regions (compared with high-gradient regions) in our mean-field simulation due to the lower density ratio at the interfaces, we can expect that the same mechanism is governing the layer merging events in the Tyrrhenian Basin. This is indeed the case. For year 1973, utilizing the thermal expansion rate and haline contraction rate of  $\alpha = 2.1 \times 10^{-4} / ^\circ\text{C}$ ,  $\beta = 7.7 \times 10^{-4} / \text{psu}$  [31], we calculate the average interface density ratio to be 1.32 in the high-gradient region (averaged over three interfaces between 750 and 850 m) and 1.03 in the low-gradient regions (averaged over four interfaces between 850 and 1400 m). For later data in year 1992, the density ratio has been evaluated by previous researchers (see TEMPO-4 data in Table 1 of Ref. [2]). The interface density ratio  $R_I$  is approximately 1.5 for layers in the higher gradient region and these are characterized by a much lower value of around 1.2 in the lower gradient region that is deeper in the water column. The systematically lower interface density ratio in the lower gradient region provides solid evidence in support of the explanation of these observations that our analyses have provided.

In the most recent analysis of data for the period 2003–2016 in Tyrrhenian Basin [30], it has been shown that the layering structure recorded above 2000 m depth has similar depth-size distribution as that been observed in 1992 in Ref. [2], with no evidence of further massive layer merging events. However, a systematic upward drift of the staircases is observed to occur, accompanied by smaller steps formed below approximately 2000 m, since May 2010. Although the reason that leads to the upward drift of the staircases remains to be explained, these newly formed smaller steps in the deep ocean are expected to correspond to the initially formed layering stage of our simulation [Fig. 5(d)], which not yet begun to merge and thus has much smaller steps compared with those in the fully merged region.

There exists other observational evidence for the layer merging process: For example, the ITP profile data analyzed in Ref. [18] serendipitously included data characterizing a single layer merging event in its entirety over a period of several days. However, the collected data lies in the diffusive-convection regime for which it is generally believed that  $\gamma$  instability theory alone can not provide a definitive explanation of the process of staircase formation (see discussions in Ref. [32], for example). In the remainder of most cases of thermohaline staircases, the staircase structure has been measured over a relatively short time period and it is therefore difficult for us to infer whether the system lies in a state that is susceptible to further layer merging or the system has already reached a relatively stable state in which no further layer merging events will occur. If the latter is the case, our analyses may still provide useful insights: If the layer merging events are susceptible to a certain type of suppression in the active ocean environment (turbulent stirring or large vertical shear, for example) so that layer merging can only occur if the growth rate is sufficiently high, our analyses demonstrate that the equilibrium step sizes have to be larger in regions with lower gradient. A more detailed analysis of the interaction between staircase formation and internal waves, for example, will be required in the process of building a fully robust understanding of thermohaline staircase formation.

## V. CONCLUSIONS

In this paper, we have developed a theoretical framework to enable analyses of the way in which the  $\gamma$  instability theory proposed in Ref. [12] must be modified in a circumstance in which the vertical gradients of temperature and salinity vary as a function of vertical position. Our theoretical framework and mean field model simulation demonstrates that, while the evolution of thermohaline staircases is still governed by the  $\gamma$  instability of Ref. [12] and the layer merging instability of Ref. [15], a series of ubiquitous features begin to appear once the inhomogeneity of background temperature and salinity gradients are considered. In the region that has lower gradient, the initial layers form and merge more quickly and finally equilibrate to a state that has higher step sizes compared with regions with relatively higher gradients. These observed differences have been explained based on a detailed analysis utilizing the mathematical properties of the  $\gamma$  instability and the layer merging instability. It has been shown that the difference in background density ratio  $R_\rho$  that is established by the coarse balance of vertical fluxes throughout the domain is the key to understanding the results obtained for these different characteristics of the staircase in high- and low-gradient regions. The structures that are observed in our mean field simulations are also found in the observed time series data of thermohaline staircases in the Tyrrhenian Basin. A detailed comparison of interface density ratios revealed that the evolution of staircases in the Tyrrhenian Basin fits exactly to our detailed scenario for staircase formation and evolution.

It must be recognized, however, that our mean-field simulations are based on a series of idealized assumptions. In particular, we have assumed that a one-dimensional mean field analysis should provide an adequate explanation of the governing dynamical processes which explicitly ignores the possible influence of horizontal gradients, for example. We have also assumed that this one-dimensional thermocline is maintained by the restoring force that is specifically chosen in our model, while in reality the maintenance of the tropical thermocline relies on the circulation driven by the complex interaction of buoyancy and winds. Furthermore, we have not included the influence of any external forcing or background turbulent mixing in the model. Although our simulation works well in providing qualitatively accurate explanations for the mechanism that leads to higher steps in the lower gradient regions, we cannot expect a simulation of this kind to fully capture the details of thermohaline staircases in the ocean. In fact, the interface density ratio in our mean field simulation obtains much higher values of 2–4 compared with oceanographically observed values of 1.1–1.8, which is a consequence of the lack of a parametrization for background turbulent mixing. The entire evolution of our mean field simulation for 100 000 nondimensional time units corresponds to a physical timescale of approximately 2 years, which is still somewhat faster than the observed layer merging events described in Ref. [2]. For the purpose of more fully describing the detailed

dynamics of staircase formation in the oceans, high-resolution basin scale models (see the example of Ref. [16]) should be employed together with an accurate representation of different sources of vertical and horizontal mixing.

### ACKNOWLEDGMENTS

The research of W.R.P. at University of Toronto is supported by NSERC Discovery Grant No. A9627. The detailed salt-fingering turbulence data sets on the basis of which the flux laws employed in this paper were produced were computed on the SciNet facility, which is a component of the Compute Canada HPC platform.

### APPENDIX A: INDIVIDUAL INFLUENCES OF NONZERO $A_3$ , $A_\Theta$ , AND $A_S$ IN THE LINEAR STABILITY ANALYSIS OF A MORE GENERALLY INHOMOGENEOUS SALT-FINGERING ENVIRONMENT

Although we have shown in the main text that the terms that are associated with variation of the temperature and salinity gradients ( $A_3$ ,  $A_\Theta$ , and  $A_S$ ) are all canceled in the linear stability analysis for our simulation initialized with hyperbolic tangent profiles for both salinity and temperature, it is still meaningful for us to specifically study the influence of each of these terms for more general cases. It should be noticed that  $\{A_1, A_2, A_3, A_S, A_\Theta, \bar{R}_\rho\}$  are all dependent on the vertical coordinate  $z$  in a vertically inhomogeneous system. However, it will be illuminating to first study the special case in which these parameters are assumed to be depth independent. In this case, (12) will be simplified into an eigenvalue problem governed by a  $2 \times 2$  matrix after expanding the perturbation fields into normal modes of the form  $e^{\lambda t + ikz}$  as in the previous subsection. The eigenvalue equation can be solved numerically for each given set of these parameters together with an assumed vertical wave number  $k$ .

In the case where  $A_3 = A_S = A_\Theta = 0$ , the system returns to the case we have described in the Sec. III A, in which growth rate is plotted as the black curve in Fig. 8(a). The growth rate is proportional to the square of the vertical wave number, which is due to the presence of the ultraviolet catastrophe in current  $\gamma$  instability theories. The depth variation of temperature and salinity gradients introduces new terms  $A_3$ ,  $A_S$ , and  $A_\Theta$  into our model. Their influences are illustrated in Fig. 8(a): The functional dependence of fastest growth rate  $\lambda$  on  $k$  is plotted in the case in which only one of these three parameters are turned on to 1 (the absolute value does not matter but simply sets the scale for  $k$ , and the negative value has the same growth rate by symmetry) and the others are set to 0. The parameters  $A_S$  and  $A_\Theta$  have exactly the same influence on the curve and therefore they are represented by the same curve in Fig. 8(a). In the large- $k$  regions ( $k \gg A_3$  or  $k \gg A_\Theta$ ), the growth rate is quadratically dependent on  $k$  for the case of both nonzero  $A_3$  and nonzero  $A_S$ , since the perturbations growing at the high order will not be sensitive to the depth variations which are relatively low order and the behavior of classical  $\gamma$  instability still governs the system. Perturbations growing at the value of  $k$  that is smaller or similar to the scales of depth variations ( $k \lesssim A_3$  or  $k \lesssim A_\Theta$ ), on the other hand, begin to express their influences through  $A_3$ ,  $A_S$ , and  $A_\Theta$ . Specifically,  $A_3$  tends to enhance the  $\gamma$  instability while  $A_S$  and  $A_\Theta$  act so as to suppress the instability, as can be seen in the blue and red curves in Fig. 8(a). While Fig. 8(a) only shows the growth rate when the criterion  $A_1 > 0$  is satisfied, we also plot the growth rate when  $A_3 = 1$ ,  $A_S = A_\Theta = 0$  in Fig. 8(b) for the case of  $A_1 = 0$  and  $A_1 < 0$  [we use the values of  $A_1 = 0.15, 0$ , and  $-0.15$  to plot Fig. 8(b)]. Again, the system well obeys the properties of the classical  $\gamma$  instability theory in the large- $k$  region: The system is unstable for  $A_1 > 0$  and becomes stable for  $A_1 \leq 0$ . In the small- $k$  regions ( $k \lesssim A_3$ ), however, the instability is determined by  $A_3$  and thus is independent of the sign of  $A_1$ .

To summarize, consideration of the depth variations of temperature and salinity gradients only significantly influence the stability of the system when the scales of the perturbations are close to the length scale for depth variations. In reality (when there is no ultraviolet catastrophe), the largest possible wave number should be truncated at the length scale below which the mean field equation

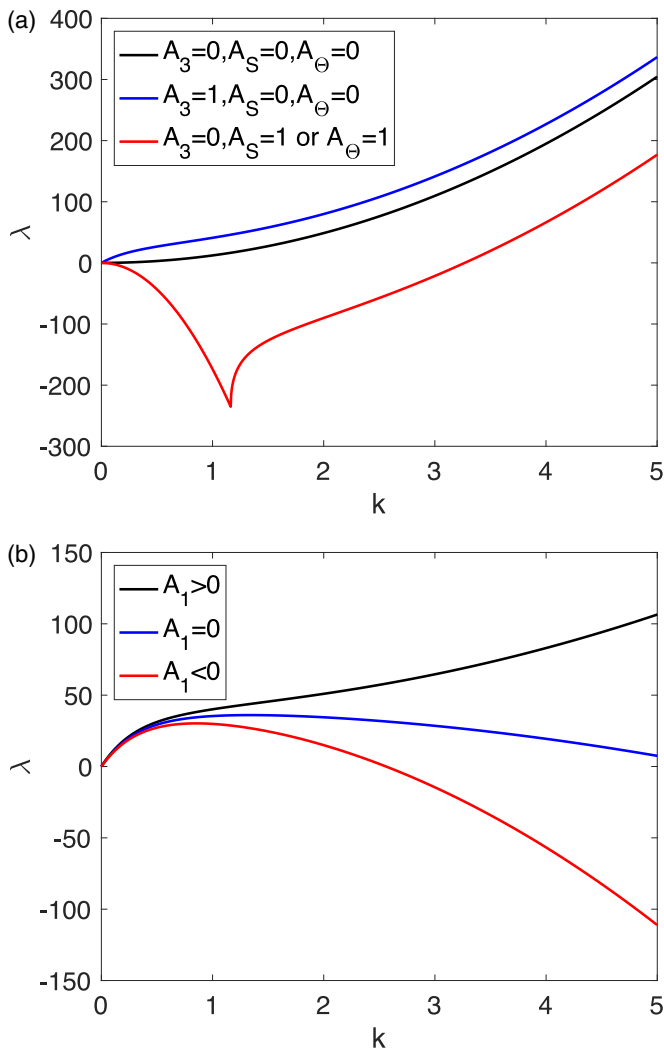


FIG. 8. The real part of growth rate as a function of vertical wave number in the cases of (a)  $A_1 > 0$  and only one of  $A_3$ ,  $A_r$ , and  $A_\theta$  is set to 1 while others are 0; and (b)  $A_3 = 1$ ,  $A_r = A_\theta = 0$ , and  $A_1 = 0.15$ ,  $-0.15$ , or 0.  $R_\rho$  is selected to be 1.5 and  $\text{Nu}(R_\rho)$  and  $\gamma(R_\rho)$  are chosen based on (1).

cease to be meaningful. Previous research reveals that such scale is more than an order of magnitude larger than an individual finger width, which is approximately several meters. The depth variations of temperature and salinity gradients in the main thermocline, on the other hand, are usually on the order of 100 m. It is for this reason that the classical  $\gamma$  instability provides a more than adequate description of the perturbations that grow in the environment of the main thermocline.

#### APPENDIX B: DISCUSSION OF THE IMPLICATIONS OF THE RESTORING FORCE INCLUDED IN THE MEAN FIELD MODEL

As discussed in the main text, we have introduced a restoring force to balance the overall vertical diffusion in the system so as to sustain the shape of our hyperbolic tangent shape profiles that are employed to model the thermocline on which staircases are observed to be trapped. As we will

demonstrate below, this term can be viewed as representing the influence of downwelling associated with Ekman pumping from the surface mixed layer as well as the upwelling of deep water in the mid-latitude ocean, with a properly chosen value for the restoring parameter  $R_0$ .

In the following discussion, we will take the evolution of the background profile for potential temperature as an example and the same argument applies for the salinity field. We first assume that the diffusion term in our model is to be balanced by the advection term associated with the upwelling and downwelling velocity  $\bar{w}(z)$  as

$$\frac{\partial \bar{\Theta}(z, t)}{\partial t} = K_{\Theta} \frac{\partial^2 \bar{\Theta}}{\partial z^2} - \bar{w}(z) \frac{\partial \bar{\Theta}}{\partial z} = 0. \quad (\text{B1})$$

We can derive the vertical velocity profile  $\bar{w}(z)$  that is needed to balance the diffusion by substituting the form of our background profile  $\bar{\Theta}(z) = \Delta \Theta \tanh(z/h)$  to obtain

$$\bar{w}(z) = K_{\Theta} \frac{\partial^2 \bar{\Theta}}{\partial z^2} \bigg/ \frac{\partial \bar{\Theta}}{\partial z} = -2 \frac{K_{\Theta}}{h} \tanh(z/h), \quad (\text{B2})$$

which is positive (represents upwelling) at the bottom half of the domain, negative (represents downwelling) at the top half of the domain, and zero at the center of the domain.

An alternative way to balance the diffusion term is to introduce a restoring force  $R(z, t)$  as we have done in our paper and write

$$\frac{\partial \bar{\Theta}(z, t)}{\partial t} = K_{\Theta} \frac{\partial^2 \bar{\Theta}}{\partial z^2} - R_0(z) [\bar{\Theta}(z, t) - \bar{\Theta}(z, 0)]. \quad (\text{B3})$$

At  $t = 0$ , it is clear that this restoring term vanishes and thus the evolution of the system is governed only by the diffusion term. After a short time period  $\delta t$ , the  $\Theta$  profile can be estimated with a first-order approximation as

$$\bar{\Theta}(z, \delta t) \approx \bar{\Theta}(z, 0) + \delta t K_{\Theta} \frac{\partial^2 \bar{\Theta}(z, 0)}{\partial z^2}. \quad (\text{B4})$$

Thus, (B3) becomes

$$\begin{aligned} \frac{\partial \bar{\Theta}(z, t = \delta t)}{\partial t} &= K_{\Theta} \frac{\partial^2 \bar{\Theta}(z, \delta t)}{\partial z^2} - R_0(z) [\bar{\Theta}(z, \delta t) - \bar{\Theta}(z, 0)] \\ &\approx K_{\Theta} \frac{\partial^2 \bar{\Theta}(z, \delta t)}{\partial z^2} - R_0(z) \delta t K_{\Theta} \frac{\partial^2 \bar{\Theta}(z, 0)}{\partial z^2}. \end{aligned} \quad (\text{B5})$$

Since  $\frac{\partial^2 \bar{\Theta}(z, \delta t)}{\partial z^2} \approx \frac{\partial^2 \bar{\Theta}(z, 0)}{\partial z^2}$ , this balance can be approximately reached if we choose  $R_0(z) = R_0 = 1/\delta t$  (which suggests that  $R_0$  should be depth independent). Thus,  $R_0$  (or  $\delta t$ ) represents the preset timescale in our system that is needed for the balance to be achieved. Although the restoring force acts as a replacement for the influence of upwelling and downwelling, the value of the timescale of the restoring force  $R_0$  is independent of the strength of upwelling and downwelling. In fact, we have to choose an appropriate value of  $R_0$  so that the strength of this restoring force is sufficient to compete with the overall diffusion but small enough to avoid suppressing the growth of the  $\gamma$  instability mode. Under the choice of the domain size and initial profiles, the nondimensional value of  $K_{\Theta} \frac{\partial^2 \bar{\Theta}(z, 0)}{\partial z^2}$  in Eq. (B4) can be estimated to be of order  $10^{-6}$ . Thus, for the approximation made in (B4) to be appropriate, the value of  $R_0 = 1/\delta t$  needs to be much higher than this value. Meanwhile, the value of  $R_0$  needs to be much smaller than the growth rate of the primary  $\gamma$  mode  $\lambda_{\max} = 1.3 \times 10^{-3}$ , suggesting a relatively narrow range of parameter values is possible, namely,

$$10^{-6} \ll R_0 \ll 10^{-3}. \quad (\text{B6})$$

We have specifically chosen  $R_0 = 10^{-5}$  in the simulation described in our main text.



- 
- [1] R. Tait and M. Howe, Some observations of thermo-haline stratification in the deep ocean, in *Deep Sea Research and Oceanographic Abstracts* (Elsevier, Amsterdam, 1968), Vol. 15, pp. 275–280.
- [2] G. Zodiatis and G. P. Gasparini, Thermohaline staircase formations in the Tyrrhenian Sea, *Deep Sea Res. Part I* **43**, 655 (1996).
- [3] R. W. Schmitt, H. Perkins, J. Boyd, and M. Stalcup, C-salt: An investigation of the thermohaline staircase in the western tropical North Atlantic, *Deep Sea Res. Part A* **34**, 1655 (1987).
- [4] R. W. Schmitt, J. Ledwell, E. Montgomery, K. Polzin, and J. Toole, Enhanced diapycnal mixing by salt fingers in the thermocline of the tropical atlantic, *Science* **308**, 685 (2005).
- [5] M.-L. Timmermans, J. Toole, R. Krishfield, and P. Winsor, Ice-Tethered Profiler observations of the double-diffusive staircase in the Canada Basin thermocline, *J. Geophys. Res.* **113**, C00A02 (2008).
- [6] T. D. Foster and E. C. Carmack, Temperature and salinity structure in the Weddell Sea, *J. Phys. Oceanogr.* **6**, 36 (1976).
- [7] S. Kimura, K. W. Nicholls, and E. Venables, Estimation of ice shelf melt rate in the presence of a thermohaline staircase, *J. Phys. Oceanogr.* **45**, 133 (2015).
- [8] C. B. Begeman, S. M. Tulaczyk, O. J. Marsh, J. A. Mikucki, T. P. Stanton, T. O. Hodson, M. R. Siegfried, R. D. Powell, K. Christianson, and M. A. King, Ocean stratification and low melt rates at the ross ice shelf grounding zone, *J. Geophys. Res.: Oceans* **123**, 7438 (2018).
- [9] R. Hoare, Thermohaline convection in Lake Vanda, Antarctica, *J. Geophys. Res.* **73**, 607 (1968).
- [10] T. Sommer, J. R. Carpenter, M. Schmid, R. G. Lueck, M. Schurter, and A. Wüest, Interface structure and flux laws in a natural double-diffusive layering, *J. Geophys. Res.: Oceans* **118**, 6092 (2013).
- [11] T. Radko, *Double-Diffusive Convection* (Cambridge University Press, Cambridge, UK, 2013).
- [12] T. Radko, A mechanism for layer formation in a double-diffusive fluid, *J. Fluid Mech.* **497**, 365 (2003).
- [13] S. Stellmach, A. Traxler, P. Garaud, N. Brummell, and T. Radko, Dynamics of fingering convection II: The formation of thermohaline staircases, *J. Fluid Mech.* **677**, 554 (2011).
- [14] E. Rosenblum, P. Garaud, A. Traxler, and S. Stellmach, Turbulent mixing and layer formation in double-diffusive convection: Three-dimensional numerical simulations and theory, *Astrophys. J.* **731**, 66 (2011).
- [15] T. Radko, What determines the thickness of layers in a thermohaline staircase? *J. Fluid Mech.* **523**, 79 (2005).
- [16] T. Radko, A. Bulters, J. Flanagan, and J.-M. Campin, Double-diffusive recipes. Part I: Large-scale dynamics of thermohaline staircases, *J. Phys. Oceanogr.* **44**, 1269 (2014).
- [17] T. Radko, Mechanics of merging events for a series of layers in a stratified turbulent fluid, *J. Fluid Mech.* **577**, 251 (2007).
- [18] T. Radko, J. Flanagan, S. Stellmach, and M.-L. Timmermans, Double-diffusive recipes. Part II: Layer-merging events, *J. Phys. Oceanogr.* **44**, 1285 (2014).
- [19] R. Muench, H. J. Fernando, and G. Stegen, Temperature and salinity staircases in the northwestern Weddell Sea, *J. Phys. Oceanogr.* **20**, 295 (1990).
- [20] R. Robertson, L. Padman, and M. D. Levine, Fine structure, microstructure, and vertical mixing processes in the upper ocean in the western Weddell Sea, *J. Geophys. Res.: Oceans* **100**, 18517 (1995).
- [21] M. Stern, T. Radko, and J. Simeonov, 3D salt fingers in an unbounded thermocline with application to the central ocean, *J. Mar. Res.* **59**, 355 (2001).
- [22] A. Traxler, S. Stellmach, P. Garaud, T. Radko, and N. Brummell, Dynamics of fingering convection I: Small-scale fluxes and large-scale instabilities, *J. Fluid Mech.* **677**, 530 (2011).
- [23] T. Radko and D. P. Smith, Equilibrium transport in double-diffusive convection, *J. Fluid Mech.* **692**, 5 (2012).
- [24] Y. Ma and W. R. Peltier, Parametrization of irreversible diapycnal diffusivity in salt-fingering turbulence using DNS, *J. Fluid Mech.* **911**, A9 (2021).
- [25] J. Y. Holyer, The stability of long, steady, two-dimensional salt fingers, *J. Fluid Mech.* **147**, 169 (1984).
- [26] T. Radko, Thermohaline layering on the microscale, *J. Fluid Mech.* **862**, 672 (2019).
- [27] W. G. Large, J. C. McWilliams, and S. C. Doney, Oceanic vertical mixing: A review and a model with a nonlocal boundary layer parameterization, *Rev. Geophys.* **32**, 363 (1994).
- [28] W. R. Peltier, Y. Ma, and D. Chandan, The KPP trigger of rapid AMOC intensification in the nonlinear Dansgaard-Oeschger relaxation oscillation, *J. Geophys. Res.: Oceans* **125**, e2019JC015557(2020).



- [29] P. Falco, M. Trani, and E. Zambianchi, Water mass structure and deep mixing processes in the Tyrrhenian Sea: Results from the vector project, [Deep Sea Res. Part I](#) **113**, 7 (2016).
- [30] S. Durante, K. Schroeder, L. Mazzei, S. Pierini, M. Borghini, and S. Sparnocchia, Permanent thermohaline staircases in the Tyrrhenian Sea, [Geophys. Res. Lett.](#) **46**, 1562 (2019).
- [31] O. M. Johannessen and O. S. Lee, A deep stepped thermohaline structure deep in the Mediterranean, [Deep Sea Res. Oceanogr. Abstr.](#) **21**, 629 (1974).
- [32] T. Radko, Thermohaline layering in dynamically and diffusively stable shear flows, [J. Fluid Mech.](#) **805**, 147 (2016).